IET Power Electronics

*Research Article*

IET Journals
The Institution of Engineering and Technology

# Reduced component, buck–boost converter for plug-in electric vehicles with a current sensing-based efficient NLCC technique

ISSN 1755-4535
Received on 1st January 2020
Revised 15th July 2020
Accepted on 3rd August 2020
E-First on 7th October 2020
doi: 10.1049/iet-pel.2020.0003
www.ietdl.org

*Anjanee Kumar Mishra*[1] ✉, *Ankit Kumar Singh*[2], *Taehyung Kim*[3]

[1]*Department of Electrical and Computer Engineering, University of Michigan-Dearborn, Dearborn, MI 48128, USA*
[2]*Department of Electrical and Instrumentation Engineering, TIET, Patiala 147004, India*
[3]*Department of Electrical and Computer Engineering, University of Michigan-Dearborn, Dearborn, MI 48128, USA*
✉ *E-mail: anj2010mishra@gmail.com*

**Abstract:** This work proposes a cost effective with a compact power electronic interface for plug-in electric vehicles (PEVs), which has the ability to achieve the all modes of vehicle operation, including plug-in charging, propulsion (PR) and regenerative braking (RB) for on-board applications. The proposed converter for PEVs has minimum component count as well as step-up and step-down operation ability depending upon the system requirement. The capability of the proposed converter to work in both the modes allows wide range of battery parameters selection, efficient DC-link voltage regulation and offers more flexibility in RB. Moreover, a current sensing based (without voltage sensor) non-linear carrier control (NLCC) technique for power factor correction has also developed in this work. This control scheme improves the reliability and stability of system by reducing the feedback circuitry. A prototype of the proposed charging system is established and analysed to an authenticate the effectiveness of developed system under steady state and dynamic conditions.

## 1 Introduction

With increasing demand of green energy, various research projects on pollution free vehicles, typically electric vehicles (EVs) and plug-in hybrid EVs (PHEVs), cumulatively known as plug-in EVs (PEVs) have gained much interest in recent years [1]. The major components of the PEVs are the battery, driving motor, controller and on-board charger (OBC) [2, 3]. The OBC uses the residential supply, i.e. 120–240 V with charging power level varying from 1.8 to 4 kW [4]. It has to be compact and lightweight because it is mounted inside the vehicle. Two types of battery chargers are typically used in OBC: (i) two-stage chargers and (ii) single-stage chargers. In two-stage chargers [5–11], a number of components (switches, diodes, passive elements, sensors, etc.) are employed to achieve variable output voltage and power factor correction (PFC) at front-stage [3, 12, 13]. The double-stage chargers involve a high number of components and, therefore, less suitable for OBC. Therefore, a reduced component count single-stage on-board battery charging system is developed by many researchers and reported in the literature [4, 14–16]. However, these chargers have one basic problem of low-frequency battery current ripple, which affects the battery life and overall performance of the system.

Generally, PEVs utilise a bidirectional DC–DC converter between a motor inverter and a battery for facilitating the power flow during the propulsion (PR) and regenerative operating modes [17–20]. To further optimise the dimension and cost of the chargers, some new single-stage integrated topologies of DC–DC converters are developed [21–25] in which the bidirectional DC–DC converter is incorporated with an add-on charger unit, to have only one DC–DC converter for all operating modes of vehicle. The integrated converter reported in [21] has the ability of step-up / down operation in each mode. However, it comprises large count of semiconductor components with a reduced efficiency and a larger size. The another integrated converters discussed in [22, 23] have buck/boost functioning in PR and regenerative braking (RB) modes nevertheless the buck operation is not obtainable in plug-in charging mode, therefore, a specific battery configuration is needed for these systems. In [26, 27], the reported integrated chargers utilise an electric motor winding and traction inverter for the charging unit through relays and mechanical switches, thereby excluding extra inductors required in the charging mode. It results in the reduced weight and size of charging unit. However, a bidirectional DC–DC converter is still needed in such systems due to requirement of suitable voltage and current magnitudes at the battery terminal under boost mode of operation. Additionally, these charging units have another limitations like need of particularly designed windings, suitable only for certain class of electric machines, less reliable due to presence of mechanical associations and control complexity. These disadvantages create difficulties in commercialisation of such charging units.

A different class of charger called quasi-two-stage charging system is also developed and reported in [28]. In this configuration, which the converter is worked as a boost mode (as a single-stage operation) when the battery terminal voltage is greater than the grid voltage and acts as a two-stage system and drawn power from the grid when the battery voltage is smaller than the grid peak voltage. However, the efficiency of overall system diminishes due to the two-stage operation. In addition, the converter utilised in the system has undergone higher conduction losses. However, the integrated converter reported in [29], has achieved both buck and boost mode operations but at the cost of three-switches and two-inductors (except inductor of filter operation). The system discuss in [30] having integrated converter comprises four-switches and two-inductors, and has buck/boost functions merely in plug-in charging mode. A Cuk converter based on-board charging system is reported in [31], which works only for charging mode. A multidevice-based interleaved boost PFC converter has been proposed in [32]. This converter has four- switches, six-diodes and two-inductors with only boosting capability. A zero voltage switching (ZVS)-based interleaved boost converter has been proposed in [33] for the efficiency improvement in plug-in charging mode using four auxiliary components, two switches, one capacitor and one inductor.

The general battery voltage range for PEVs is 200–450 V [34, 35]. Since, the universal grid has the voltage range of 90–260 V and, therefore, both the buck and boost operating modes are obligatory for charging/discharging of battery. Besides, the battery voltage required boosting operation (level of DC-link voltage) in the PR working mode to propel the motor drive. In high state-of-charge (SOC) situation when the battery voltage is more with respect to DC-link voltage, the buck operation of a battery is compulsory [23]. Likewise, in RB mode, buck functioning is

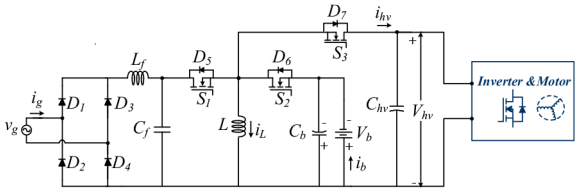


**Fig. 1** *Developed integrated converter for PEVs battery charger*

**Table 1** States of semiconductor devices in each mode

| Mode of operation | Fig. | $S_1$ | $S_2$ | $S_3$ | $D_5$ | $D_6$ | $D_7$ |
|---|---|---|---|---|---|---|---|
| plug-in charging | Fig. 2*a* | PWM | OFF | OFF | OFF | OFF | OFF |
| | Fig. 2*b* | OFF | OFF | OFF | OFF | ON | OFF |
| PR | Fig. 4*a* | OFF | PWM | OFF | OFF | OFF | OFF |
| | Fig. 4*b* | OFF | OFF | OFF | OFF | OFF | ON |
| RB | Fig. 4*c* | OFF | OFF | PWM | OFF | OFF | OFF |
| | Fig. 4*d* | OFF | OFF | OFF | OFF | ON | OFF |

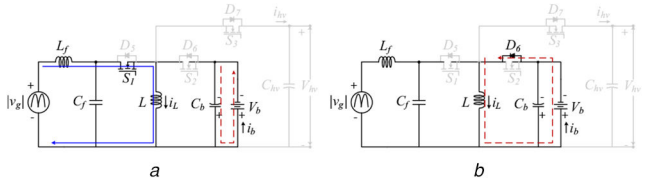

**Fig. 2** *Operation of converter during the plug-in charging when*
***(a)*** Switch $S_1$ is ON, ***(b)*** Switch $S_1$ is OFF

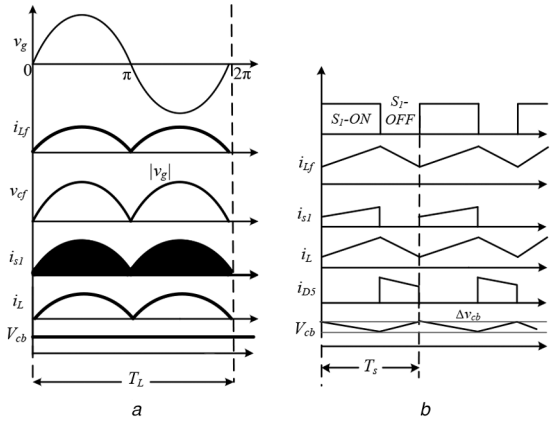


**Fig. 3** *Associated waveforms of the proposed converter during the plug-in charging mode*
***(a)*** Over one line cycle, ***(b)*** Over one switching cycle

characteristically needed because the DC-link voltage is typically greater or closely to the battery terminal voltage [21]. However, at lower drive speeds, the boost operation of converter is critically required to receive all the energy back to the system which is generated in RB mode [22]. Thus, the above discussion clearly concludes that the DC–DC converters having buck–boost operating capability are only capable to achieve the all working modes successfully and suitable for PEVs.

Therefore, acknowledging all the limitations of conventional charging systems, a new integrated DC–DC converter for PEVs utilising a cminimum number of components counts (three-switches, one-inductor and two-capacitors) is proposed in this paper. The schematic diagram of the proposed charging system is shown in Fig. 1. The proposed converter has buck/boost operating capability for each mode with simpler control strategy due to conduction of only one switch during each mode of operation. Further, a non-linear carrier control (NLCC) technique is used to obtain the PFC and to maintain the required power quality at the grid side. The implemented control strategy does not need any voltage sensor and only single current sensor is required for its implementation. The proposed integrated DC–DC converter has the small count of components compared to existing integrated DC–DC converters and conventional DC–DC converter, which makes the system compact, cost effective and light in weight and suitable for light EVs (LEVs) such as e-scooters (standing/self-balancing and folding types), e-bikes, e-golf carts, e-rickshaws, and other types of e-three-wheelers.

Continuing sections of this paper are planned as follows: Section 2 discusses the operation modes of the converter. In Section 3, the selection of passive components is discussed to ensure the continuous conduction mode (CCM) of operation. The loss calculation of proposed converter in AC–DC and DC–DC stage is discussed in Subsection 2.3. Subsection 2.4 establishes the comparison among the proposed converter, conventional converters, and integrated converters. In Section 3, the control strategy for different modes are discussed. The examination of captured simulation and hardware results has been done in Section 4. Finally, the concluding observations obtained from the study are mentioned in Section 5.

## 2 Principle of the proposed converter

### *2.1 Fundamental operational principle of the proposed converter*

The proposed converter shown in Fig. 1 has three basic modes of operation, namely plug-in charging, PR and RB. The operation of each mode is described as follows. The states of semiconductor devices in each mode are given in Table 1.

*2.1.1 Plug-in charging mode:* This mode begins by assembling a utility grid to the charging system. Concurrently, the proposed converter sustains the desired power quality at the grid side. In this operating mode, switch $S_1$ is active and switches $S_2$ and $S_3$ are open circuited. The battery is being charged from the utility grid and at the same time the proposed converter operates in the PFC mode. The operation of converter in one switching cycle with relevant waveforms is discussed in Figs. 2 and 3.

When the switch $S_1$ turns-ON, the inductor $L$ is charged through the path $|v_g| - L_f - S_1 - |v_g|$, as shown in Fig. 2*a*, and current through $L$, i.e. $i_L$ is linearly increasing. Meanwhile the capacitor $C_b$ supplies energy to the battery, and the voltage across capacitor $C_b$ ($V_{cb}$) decreases, as illustrated in Fig. 3*b*. When the switch $S_1$ turns-OFF, the inductor $L$ transfers its energy to the capacitor $C_b$ and the battery, as shown in Fig. 2*b*. For one line and switching cycles, the waveforms of this mode are shown in Figs. 3*a* and *b*, respectively. If the duty ratio of the switch $S_1$ is $d_1$, by applying volt-second balance through the inductor $L$ in a switching period $T_s$ can be written as

$$V_{g\max} \mid \sin(\omega t) \mid * d_1(t) * T_s = -V_b * (1 - d_1(t)) * T_s \quad (1)$$

From (1), the voltage conversion ratio, $M_1$ is defined as

$$M_1 = \frac{V_b}{V_{g\max}|\sin \omega t|} = -\frac{d_1(t)}{1 - d_1(t)} \quad (2)$$

*2.1.2 PR mode:* In PR mode, power flows from the battery to DC link for propelling of motor–drive system, and switches $S_1$ and $S_3$ are in OFF-state and switch $S_2$ is PWM gated. When the switch $S_2$ is turned-ON, the battery charges the inductor $L$ through the path $V_b$–$L$–$S_2$–$V_b$, as shown in Fig. 4*a*. Meanwhile, the capacitor $C_{hv}$ discharges by supplying energy to the motor through an inverter. When the switch $S_2$ is turned-OFF, stored energy in $L$ is transfered

to the DC-link capacitor $C_{hv}$ through the path $L$–$D_7 - C_{hv}$–$L$, as depicted in Fig. 4*b*. If the duty ratio of the converter is $d_2$, then by applying the volt-second balance through the inductor $L$, the following equation is obtained:

$$V_{\mathrm{b}} * d_2 * T_{\mathrm{s}} = -V_{hv} * (1 - d_{\mathrm{d}}) * T_{\mathrm{s}} \tag{3}$$

Then, the voltage conversion ratio $M_2$ from (3) can be expressed as

$$M_2 = \frac{V_{hv}}{V_{\mathrm{b}}} = -\frac{d_2}{1 - d_2} \tag{4}$$

*2.1.3 RB mode:* This mode helps in a longer run of vehicle by utilising braking energy of the drive to charge the battery. In this mode, switches $S_1$ and $S_2$ are in OFF-state and switch $S_3$ is gated through a pulse-width modulation (PWM) signal. By turning-ON switch $S_3$, the inductor $L$ begins charge through the path $V_{hv} - S_3 - L_2 - V_{hv}$, as shown in Fig. 4*c*. When the switch $S_3$ turns-OFF, $L$ releases its stored energy to the capacitor $C_{\mathrm{b}}$ and battery, which is shown in Fig. 4*d*. If the duty ratio of the converter is $d_3$ by applying the volt-second balance through the inductor $L$ the following form is obtained:

$$V_{hv} * d_3 * T_{\mathrm{s}} = -V_{\mathrm{b}} * (1 - d_{\mathrm{d}}) * T_{\mathrm{s}} \tag{5}$$

The voltage conversion ratio $M_3$ from (5) can be expressed as

$$M_3 = \frac{V_{\mathrm{b}}}{V_{hv}} = -\frac{d_3}{1 - d_3} \tag{6}$$

### 2.2 Components selection

In this section, the selection of passive components is discussed. The design basis of the components is, to satisfy the CCM operation and ripple minimisation in the voltage and current.

*2.2.1 Selection of inductor L:* The inductor $L$ is utilised in each mode hence, its value is determined in each mode, and the largest value from all modes will be chosen as the final value for the CCM operation of the converter. The inductor value in any mode for the CCM operation, is given as [13]

$$L_{\mathrm{CCM}} > \frac{V_{\mathrm{out}}}{P_{\mathrm{out}}} \frac{(1 - d)^2}{2 f_{\mathrm{s}}} \tag{7}$$

where $V_{\mathrm{out}}$, $P_{\mathrm{out}}$, $d$ and $f_{\mathrm{s}}$ denote output voltage, output power, duty cycle and switching frequency, respectively. The selected value of $L$ in the simulation and hardware is 2 mH.

The winding thickness and core size of an inductor rely upon the maximum current and flux density. The peak flux density relies upon the maximum current flowing through the inductor; subsequently, both winding thickness and core size of the inductor rely upon the maximum current flowing through it [22]. The inductor $L$ is used in all modes and the power level of the PR mode is generally a lot higher when contrasted with different methods of vehicle and hence the size of $L$ is primarily estimated by the PR mode.

*2.2.2 Estimation of capacitor $C_{\mathrm{b}}$:* The size of battery terminal capacitor $C_{\mathrm{b}}$ is given by the following equation [36]:

$$C_{\mathrm{b,min}} > \frac{P_{\mathrm{b}}}{4 f_{\mathrm{L}} \Delta v_{\mathrm{b}} V_{\mathrm{b}}} \tag{8}$$

where $f_{\mathrm{L}}$ is the grid frequency and $\Delta v_{\mathrm{b}}$ is the capacitor voltage ripple. In a single-stage charger, a low-frequency ripple (100 Hz) appears at the output stage [37]. To mitigate this low-frequency ripple at the output stage, a higher value of the capacitor is chosen, however, it leads to increase the size of the electrolytic capacitor. Thus, the trade-off between ripple across output voltage and capacitor size must be taken into consideration for designing the converter.

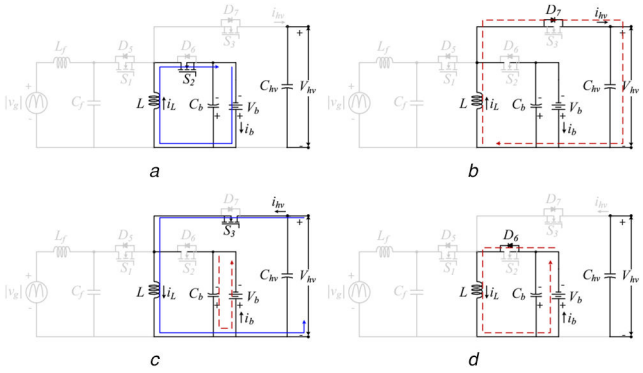


**Fig. 4** *Converter operation in*
***(a)*** PR mode, when switch $S_2$ is active, ***(b)*** When switch $S_2$ is open, ***(c)*** RB mode, when $S_3$ is active, ***(d)*** When $S_3$ is open

*2.2.3 Selection of filter components, $L_{\mathrm{f}}$ and $C_{\mathrm{f}}$:* The selection of filter components is necessary for obtaining small harmonic distortion in grid current [38, 39]. The peak magnitude of $C_{\mathrm{f}}$ is expressed as

$$C_{f_{\max}} = \frac{I_{\mathrm{g,max}} \tan(\theta)}{2\pi f_L V_{\mathrm{g,max}}} \tag{9}$$

where $V_{\mathrm{g,max}}$, $I_{\mathrm{g,max}}$ and $f_L$ are peak grid voltage, peak grid current, and line frequency, respectively, and $\theta$ is selected below 5° for a large input power factor. The $C_{\mathrm{f_{max}}}$ is estimated as 1.14 $\mu$F and chosen size in the simulation and hardware is 1 $\mu$F.

The value of inductor, $L_{\mathrm{f}}$ is given as

$$L_{\mathrm{f}} = \frac{1}{4\pi^2 f_{\mathrm{c}}^2 C_{\mathrm{f}}} \tag{10}$$

where $f_{\mathrm{c}}$ is the cut-off frequency of deigned filter which is selected as it should be more than the grid frequency ($f_1$ = 50 Hz) and less than the switching frequency ($f_{\mathrm{s}}$ = 20 kHz). Therefore, $f_{\mathrm{c}}$ is chosen as 4 kHz. The $L_{\mathrm{f}}$ from (10) is calculated as 1.58 mH and the selected value in the simulation and hardware is 1.5 mH.

### 2.3 Loss analysis

An analytical loss calculation of the proposed converter that includes losses of semiconductors and losses of passive components are investigated in this section. In addition, for the loss calculation given in Table 2, the analytical current equations ((root mean square (RMS) and average) for semiconductor devices and passive components are required.

(a) *Switch conduction loss:* The conduction loss for a MOSFET switch is determined as

$$P_{\mathrm{S,cond}} = I_{\mathrm{s,RMS}}^2 * R_{(\mathrm{ds})} \tag{11}$$

while the conduction loss for an IGBT switch is estimated as

$$P_{\mathrm{S,cond}} = \langle i_{\mathrm{s}} \rangle_{Ts} * V_{CE_{\mathrm{sat}}} \tag{12}$$

(b) *Switching losses:* The switching power losses of a switch can be approximately calculated as

$$P_{\mathrm{sw}} = \frac{1}{2}(V_{\mathrm{s,max}} * I_{\mathrm{s,max}}) * (t_{\mathrm{r}} + t_{\mathrm{f}}) * f_{\mathrm{s}} \tag{13}$$

where $V_{\mathrm{s,max}}$ and $I_{\mathrm{s,max}}$ are the maximum values of voltage and current, respectively. The $t_{\mathrm{r}}$ and $t_{\mathrm{f}}$ are the rise and fall times of the selected switch, respectively.

**Table 2** RMS and average current expression of switches, diodes and inductors in each mode

| Device | Plug-in charging | | PR | | RB | |
|---|---|---|---|---|---|---|
| | RMS | Average | RMS | Average | RMS | Average |
| $S_1$ | $I_{g,RMS}\sqrt{1+\alpha\frac{8}{3\pi}}$ | $I_{g,RMS}\frac{2\sqrt{2}}{\pi}$ | NC | | | |
| $S_2$ | NC | | $\sqrt{\frac{d_2 I_{hv}^2}{(1-d_2)^2}+\frac{d_2(1-d_2)^2V_{hv}^2}{12f_s^2L^2}}$ | $\frac{d_2}{1-d_2}I_{hv}$ | NC | |
| $S_3$ | NC | | | | $\sqrt{\frac{d_3 I_{b,reg}^2}{(1-d_3)^2}+\frac{d_3(1-d_3)^2V_b^2}{12f_s^2L^2}}$ | $\frac{d_3}{1-d_3}I_{b,reg}$ |
| $D_6$ | $I_{b,grid}\sqrt{\frac{3}{2}+\frac{16}{3\pi}\alpha}$ | $I_{b,grid}$ | NC | | $\frac{I_{hv}}{\sqrt{1-d_2}}$ | $I_{b,reg}$ |
| $D_7$ | NC | | $\frac{I_{b,reg}}{\sqrt{1-d_2}}$ | $I_{hv}$ | NC | |
| $L_f$ | $I_{g,RMS}$ | $I_{g,RMS}\frac{2\sqrt{2}}{\pi}$ | NC | | | |
| $L$ | $I_{g,RMS}\sqrt{1+\frac{3}{4}\alpha^2+\frac{16}{3\pi}\alpha}$ | $I_{g,RMS}(\frac{\alpha\sqrt{2}}{2}+\frac{2\sqrt{2}}{\pi})$ | $\frac{I_{hv}}{1-d_2}\sqrt{1+\frac{R^2(1-d_2)^2}{12L^2f_s^2}}$ | $\frac{I_{hv}}{1-d_2}$ | similar to PR | |

where NC, Not conducting; $\alpha$, $V_{g,max}/V_b$; $I_{hv}$, DC-link current; $I_{b,grid}$, battery current in plug-in mode and $I_{b,reg}$, battery current in regenerative mode.

**Table 3** Semiconductor and passive components losses of the proposed converter in AC–DC and DC–DC stages with $V_b = 300$ V and $V_{hv} = 400$ V

| | | | Total semiconductors losses $P_s$, W | | Total passive components losses $P_p$, W | |
|---|---|---|---|---|---|---|
| $P_{chg}$, kW | $P_{DC-DC}$, kW | $V_{grid}$, V | AC–DC stage [plug-in charging] | DC–DC stage [PR] | AC-DC stage [plug-in charging] | DC–DC stage [PR] |
| 1.8 | 5 | 120 | 79.76 | 66.56 | 60.98 | 90.8 |
| 3.2 | 5 | 240 | 91.27 | 66.56 | 84.47 | 90.8 |
| 1.8 | 10 | 120 | 79.76 | 164.95 | 60.98 | 361.65 |
| 6.6 | 10 | 240 | 213.83 | 164.95 | 313.08 | 361.65 |

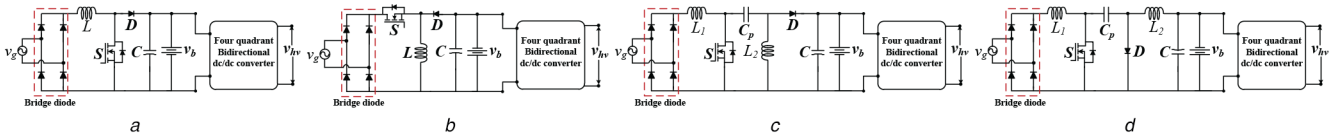


**Fig. 5** *Conventional single-stage battery chargers*
***(a)*** Boost PFC converter, ***(b)*** Inverting buck/boost PFC converter, ***(c)*** SEPIC PFC converter, ***(d)*** CuK PFC converter

(c) *Diode losses:* Power losses of a diode are the sum of diode conduction loss (product of average current and knee voltage) and reverse recovery loss and modelled as

$$P_D = V_{FD} * I_{FD} + P_{Qrr} \tag{14}$$

where $P_{Qrr}$ is the reverse recovery loss of a diode. The above expression of diode losses is used for the rectifier diodes and body diodes of switches.

Then total losses, $P_s$ of the semiconductor devices in any mode can be written as

$$P_s = P_{S,cond} + P_{sw} + P_D \tag{15}$$

(d) *Passive components losses:* The passive components that are in the main current path are $L_f$ and $L$, then inductor copper losses are modelled as

$$P_p = I_{L_f,rms}^2 * r_f + I_{L,rms}^2 * r \tag{16}$$

where $r_f$ and $r$ are series resistance of inductors $L_f$ and $L$, respectively.

Table 3 shows the total semiconductor devices losses $P_s$ and passive components losses $P_p$ in the plug-in charging (AC–DC stage) and PR (DC–DC stage), where $P_{chg}$ and $P_{DC-DC}$ are the power rating of plug-in charging and PR modes, respectively. From Table 3, it is seen that in the plug-in charging mode, the $P_s$ with a grid voltage of 240 V is around 2.8–3.2% of the rated power (3.2 and 6.6 kW). With 120 V grid, the $P_s$ in the plug-in charging is 4.3% of the rated power (1.8 kW). The $P_s$ in the DC–DC stage is between 1.3 and 1.6% of the rated power (5 and 10 kW loads). The $P_s$ in the DC–DC stage is relatively lower than the AC–DC stage because in DC–DC stage, the diode bridge losses are absent. It is also observed that the $P_p$ in the AC–DC stage is higher than the DC–DC stage because of the absence of filter inductor ($L_f$) copper loss in the DC–DC stage. Moreover, the total losses ($P_s + P_p$) in the AC–DC and DC–DC stages are between 5.4–8.2 and 3.1–5.2%, respectively.

### 2.4 Comparative analysis

The proposed converter is compared to conventional single-stage converters (Fig. 5). To establish an adequate comparison of the proposed converter with these single-stage converters, a four-quadrant bidirectional DC–DC converter is connected between the battery and DC link, as illustrated in Fig. 5. It is seen that the proposed converter has the fewer number of components compared to all conventional converters and integrated converters with buck/boost operation, as indicated Table 4.

The efficiency curves of the proposed converter and integrated converters [21, 25] are shown in Fig. 6 with 220 V grid. These integrated converters [21, 25] have buck/boost operations in each mode same as the proposed converter. The proposed converter has higher efficiency than an integrated converter [21] because in [21], there are 3–4 semiconductor devices (depending on the modes) in the main current path, as a result, conduction losses are high in each mode. In [25], there are two additional passive components in the main current path compared to the proposed converter. The

**Table 4** Comparative study of the proposed integrated converter with single-stage chargers

| Charger topologies | Mode of operation | | | Number of components | | | | |
|---|---|---|---|---|---|---|---|---|
| | Plug-in charging | PR | RB | Switch | Diode | Inductor | Capacitor | Sensor (voltage and current) |
| boost PFC converter | boost | buck/boost | buck/boost | 5 | 5 | 2 | 2 | 5 |
| inverting buck/boost PFC Converter | buck/boost | buck/boost | buck/boost | 5 | 5 | 2 | 2 | 5 |
| SEPIC PFC converter | buck/boost | buck/boost | buck/boost | 5 | 5 | 3 | 3 | 5 |
| CuK PFC converter | buck/boost | buck/boost | buck/boost | 5 | 5 | 3 | 3 | 5 |
| Integrated converter [21] | buck/boost | buck/boost | buck/boost | 6 | 9 | 1 | 2 | 4 |
| integrated converter [22] | boost | buck/boost | buck /boost | 4 | 4 | 1 | 2 | 4 |
| integrated converter [23] | boost | buck/boost | buck /boost | 4 | 4 | 2 | 3 | 5 |
| integrated converter [25] | buck/boost | buck/boost | buck/boost | 3 | 4 | 2 | 3 | 5 |
| integrated converter [30] | buck/boost | boost | buck | 3 | 4 | 2 | 3 | 5 |
| proposed integrated converter | buck/boost | buck/boost | buck/boost | 3 | 4 | 1 | 2 | 4 |

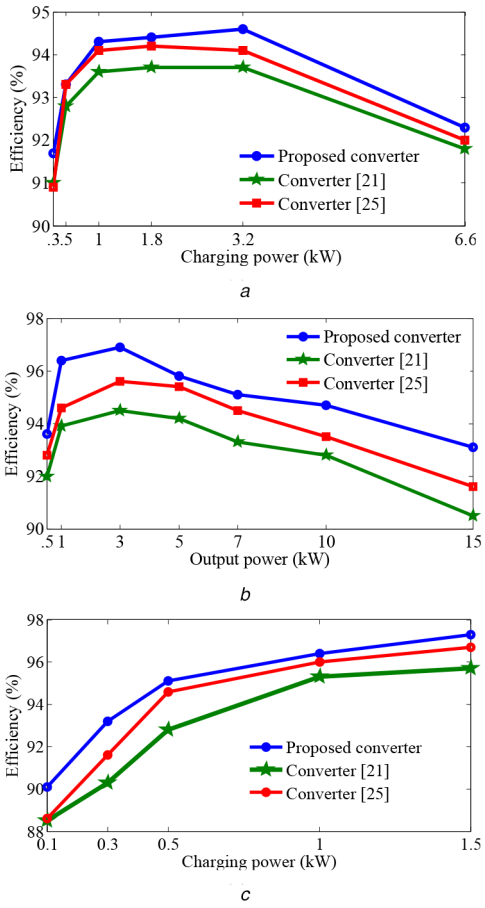


**Fig. 6** *Efficiency curves in*
***(a)*** Plug-in charging, ***(b)*** PR, ***(c)*** RB modes

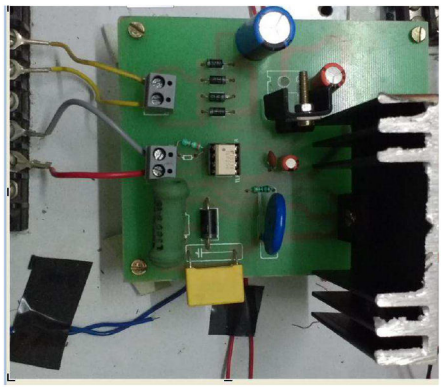

**Fig. 7** *Driver circuit of switch*

calculated peak efficiency of the proposed converter in the plug-in charging, PR and RB modes is 94.6, 96.9 and 97.2%, respectively. The proposed converter has a lower efficiency in each mode as compared to integrated converters [22, 23] because it has high voltage/current stresses on semiconductor devices and high current stress on the inductor ($L$).

Furthermore, from the size and power density point of view, the proposed converter has smaller size and higher power density compared to converters [21, 25, 30]. In [21], there are six-switches (twice of the proposed converter) and nine diodes. Switches with driver circuit occupy a considerable floor area (Fig. 7); therefore, the volume of this converter is higher and power density will be lower. Integrated converters [25, 30] have one extra sensor and two additional passive components compared to the proposed converter; therefore, the overall size of these converters will be more in comparison with the proposed converter. Integrated converters [22, 23] have low stresses in each mode with an additional switch. However, low stresses results in higher efficiency compared to the proposed converter. Therefore, heat sink requirements are comparatively lower [40] than the proposed converter, as a result, power density will be high.

## 3 Control and stability analysis

In this section, control algorithms and stability analysis are discussed. The control structure during various working modes of converter is illustrated in Figs. 8 and 9. Each mode is realised by mode selector logic, which needs an external input, such as torque ($\tau$), speed ($\omega$), and charging power ($P_g$). Since this work is focused on the power electronic converter parts of EV the mode selection is done manually.

### *3.1 PFC using NLCC method*

There are many closed-loop controlled techniques reported in the literature [41–45] to improve the power quality at the grid side in PEVs, such as average current-based control, current programmed technique, sliding mode method, etc. Generally, these conventional control techniques need both voltage and current information to achieve PFC at the grid side. However, the present charging system with the proposed integrated converter utilised NLCC technique to maintain the power quality at the grid side and there is a need of only current sensing circuit to realise this control. The elimination of voltage sensing circuit offers a decreased dimension of the charging system and improves the dynamic performance of the overall system with cost-reduction.

The main idea behind the developed NLCC method for present system is to produce a signal which is proportional to the integration of switch current (current through $S_1$) and comparing it with a reference signal $v_c$ the desired PWM pulses are created as represented in Fig. 8. The switch is active at the starting of the switching period ($T_s$). Meanwhile, integral of switch current ($i_{s1}$) is estimated utilising an operational amplifier dependent integrator, which transforms it into voltage a signal $v_i$. The $v_i$ is combined by a

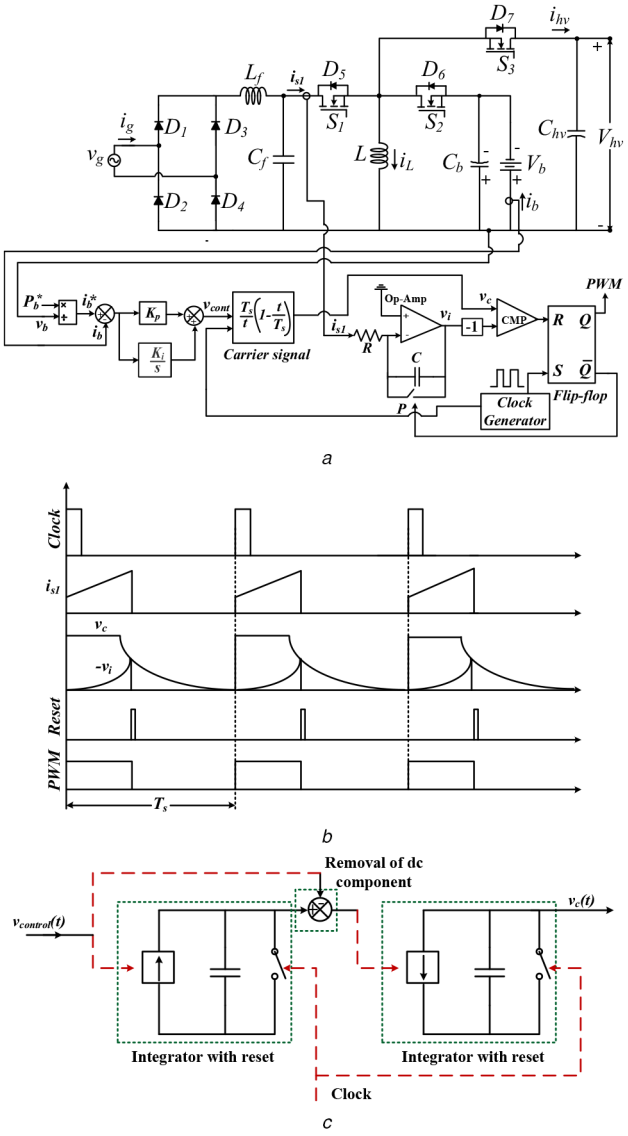


**Fig. 8** *Control strategy of the proposed system in plug-in charging mode*
***(a)*** Controller diagram during plug-in charging mode, ***(b)*** Its operation waveforms, ***(c)*** Generation of parabolic carrier signal using double integration method

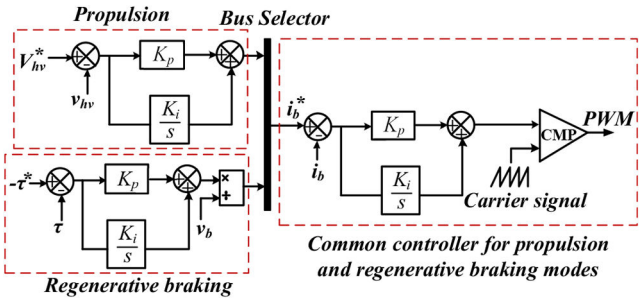


**Fig. 9** *Controller diagram during the PR and RB modes*

negative unit signal to eliminate the inversion of $v_i$ due to the operational amplifier

$$v_i(t) = -\frac{1}{RC}\int_0^{d_1T_s} i_{s1}(\tau)\,\mathrm{d}\tau 0 < t < d_1T_s \tag{17}$$

The integrator voltage $v_i(t)$ should be fixed to zero at the end of each switching cycle, and the fresh integration process starts at the beginning of the next switching period. The voltage $v_i(d_1T_s)$ is the proportional to the average switch current

$$v_i(d_1T_s) = -\frac{\langle i_{s1}\rangle_{T_s}}{RCf_s} 0 < t < T_s \tag{18}$$

To regulate the average value of current flowing through the switch, it is required to estimate the average grid current by an emulated input resistance

$$\langle i_g(t)\rangle_{T_s} = \frac{\langle v_g(t)\rangle_{T_s}}{R_e(v_{cont})} \tag{19}$$

It is further obligatory to eliminate the sensing of $v_g(t)$ and $i_g(t)$. These parameters are represented with sensed feedback variables $V_b$ and $i_{s1}$. Then we can obtain

$$\langle i_{s1}(t)\rangle_{T_s} = d_1(t)\langle i_g(t) + i_b(t)\rangle_{T_s} \tag{20}$$

which yields

$$\langle i_{s1}(t)\rangle_{T_s} = \langle i_g(t)\rangle_{T_s} \tag{21}$$

and

$$\langle v_g(t)\rangle = \frac{1-d_1(t)}{d_1(t)}V_b \tag{22}$$

Using (19), (21) and (22), the following equation is obtained:

$$\langle i_{s1}(t)\rangle_{T_s} = \frac{[1-d_1(t)]V_b}{d_1(t)R_e(v_{cont})} \tag{23}$$

By replacing $d_1(t)$ with $t/T_s$, the average current of switch can be controlled with a control voltage through non-linear carrier waveform as follows:

$$v_c(t) = v_{cont}(t)\frac{T_s}{t}\left(1-\frac{t}{T_s}\right) 0 < t < T_s \tag{24}$$

This non-linear reference voltage is valid between $0 < t < T_s$ and should be set to zero at the end of the switching period, i.e. $v_c(t+T_s) = v_c(t)$, as shown in Fig. 8*b*. A simple way to generate a parabolic carrier signal is to use two integrators as shown in Fig. 8*c*. The slow varing control signal $v_{control}(t)$ is integrated into obtain a ramp signal $v_r(t)$ and the DC component in ramp signal is removed and integrated again. The output of second integrator is a parabolic carrier signal $v_c(t)$. Both integrators are reset to zero at the end of each switching period using a clock signal. The amplitude of $v_c(t)$ hence emulated resistance is controlled by $v_{control}(t)$. Fig. 8*a* shows that the outer closed-loop controls the reference charging power and sets the amplitude of non-linear carrier waveform. The reference carrier waveform given by (24) is compared to the integral of switch current and generated PWM signal is applied to the switch $S_1$ through the driving circuit.

### 3.2 PR and RB mdes

The control objective for the PR mode is to maintain DC-link voltage constant for efficient working of the vehicle drive arrangement. The PR mode employs dual-loop PI structure, as shown in Fig. 9. The error between a reference DC-link voltage $v_{hv}$ and a sensed DC-link voltage $v_{hv}$ is given to the outer loop PI controller. The error signal between generated signal (reference battery current $i_b$) from outer controller and measured battery current $i_b$ is supplied to the inner PI controller. The output of the inner PI controller is compared to the high-frequency sawtooth carrier signal for generation of PWM pulses for the switch $S_1$.

The control strategy for the RB mode utilises either torque or speed of the vehicle drive as an input reference. This mode also utilises a dual-loop PI controller, as shown in Fig. 9. The output of the outer PI controller is a reference charging power, which produces a reference battery current (reference power/battery

voltage) for the inner current controller. The inner PI controller is common for the PR and RB modes. The output and inner controllers are compared with a sawtooth carrier signal to generate PWM pulses to switch $S_2$.

### 3.3 Stability analysis

The proposed converter operates as an inverting buck/boost converter in each mode. In the PR and RB modes, the proposed converter is a third-order system, while in the plug-in charging mode it is a second-order system. In the following paragraphs, stability and bandwidth analyses of the PR (or driving) and the plug-in charging modes are discussed using frequency response analysis, i.e. Bode plot. The stability analysis through Bode plot requires a transfer function of the converter between desired input and output. To obtain the various transfer functions of the converter state-space modelling approach is used.

In PR mode, the input and output voltages of the converter are $V_{\rm b}$ and $V_{hv}$, respectively. To simplify the modelling and stability analyses, a resistive load $R$ is connected across DC-link capacitor $C_{hv}$. The equivalent series resistance of inductor $L$, capacitors $C_{\rm b}$ and $C_{hv}$ are $r$, $r_{\rm cb}$ and $r_{\rm ch}$, respectively. In each switching period, the power stage dynamics can be described by a set of state-space equations [46], which are given by

$$\dot{x} = A_k \boldsymbol{x} + B_k u \tag{25}$$

$$y = C_k \boldsymbol{x} + D_k u \tag{26}$$

where $\boldsymbol{x} = [i_{\rm L} V_{\rm cb} V_{\rm ch}]^{\rm T}$ are the state vectors, $u = V_{\rm b}$, $y = [i_{\rm b}\ \ V_{hv}]$ and $k = 1$ and 2 for mode-1 and mode-2, respectively. The mode-1 and mode-2 denote $S_2$ ON and OFF, respectively.

Using the state-space analysis, system matrices for both modes are given as

$$\boldsymbol{A}_1 = \begin{pmatrix} -\frac{r}{L} & 0 & 0 \\ 0 & -\frac{1}{r_{\rm cb}C_{\rm b}} & 0 \\ 0 & 0 & -\frac{1}{C_{hv}(R+r_{\rm ch})} \end{pmatrix}, \quad \boldsymbol{B}_1 = \begin{pmatrix} \frac{1}{L} \\ \frac{1}{r_{\rm cb}C_{\rm b}} \\ 0 \end{pmatrix}$$

$$\boldsymbol{A}_2 = \begin{pmatrix} -\frac{r}{L} - \frac{R}{L(R+r_{\rm ch})} & 0 & -\frac{R}{L(R+r_{\rm ch})} \\ 0 & -\frac{1}{r_{\rm cb}C_{\rm b}} & 0 \\ \frac{R}{C_{hv}(R+r_{\rm ch})} & 0 & -\frac{1}{C_{hv}(R+r_{\rm ch})} \end{pmatrix}$$

$$\boldsymbol{B}_2 = \begin{bmatrix} 0 \\ \frac{1}{r_{\rm cb}C_{\rm b}} \\ 0 \end{bmatrix}$$

$$\boldsymbol{C}_1 = \begin{pmatrix} 1 & -\frac{1}{r_{\rm cb}} & 0 \\ 0 & 0 & \frac{R}{(R+r_{\rm ch})} \end{pmatrix}, \ \boldsymbol{D}_1 = \begin{bmatrix} \frac{1}{r_{\rm cb}} \\ 0 \end{bmatrix}$$

$$\boldsymbol{C}_2 = \begin{pmatrix} 0 & -\frac{1}{r_{\rm cb}} & 0 \\ \frac{r_{\rm ch}R}{(R+r_{\rm ch})} & 0 & \frac{R}{R+r_{\rm ch}} \end{pmatrix}, \ \boldsymbol{D}_2 = \begin{bmatrix} -\frac{1}{r_{\rm cb}} \\ 0 \end{bmatrix}$$

Applying the state-space averaging technique and upon simplification results the average model [46] $\dot{x} = \boldsymbol{A}\boldsymbol{x} + \boldsymbol{B}u$ and $y = \boldsymbol{C}\boldsymbol{x} + \boldsymbol{D}u$, where $\boldsymbol{A} = d_2\boldsymbol{A}_1 + (1-d_2)\boldsymbol{A}_2$, $\boldsymbol{B} = d_2\boldsymbol{B}_1 + (1-d_2)\boldsymbol{B}_2$, $\boldsymbol{C}$ and $\boldsymbol{D}$ are also expressed similar to matrices $\boldsymbol{A}$ and $\boldsymbol{B}$.

To analyse the stability of the converter, a small-signal transfer function of battery current and output voltage with respect to control signal ($d_2$) need to be obtained. The small-signal transfer function on the control signal to battery current, $G_{i_{\rm b}d}$(s) and control signal to output voltage, $G_{v_{\rm h}d}$(s) can be obtained by the following equations:

$$G_{i_{\rm b}d}(s) = C(1,:)(sI - \boldsymbol{A})^{-1}\alpha + p \tag{27}$$

$$G_{v_{\rm h}d}(s) = C(2,:)(sI - \boldsymbol{A})^{-1}\alpha + p \tag{28}$$

where $\alpha = (\boldsymbol{A}_1 - \boldsymbol{A}_2)\boldsymbol{X} + (\boldsymbol{B}_1 - \boldsymbol{B}_2)U]$ and $p = [(\boldsymbol{C}_1 - \boldsymbol{C}_2)\boldsymbol{X} + (\boldsymbol{E}_1 - \boldsymbol{E}_2)\boldsymbol{U}]$.

The outer voltage to current transfer function, $G_{v_{\rm h}i_{\rm b}}(s)$ can be obtained as

$$G_{v_{\rm h}i_{\rm b}}(s) = \frac{G_{v_{\rm h}d}(s)}{G_{i_{\rm b}d}(s)} \tag{29}$$

The set of equilibrium points of the converter is given by the following equation:

$$\boldsymbol{X} = -\boldsymbol{A}^{-1}\boldsymbol{B}\boldsymbol{U} \tag{30}$$

With $r_{\rm cb} = 0.01$, $r_{\rm ch} = 0.01$, $L = 4\,mH$, $r = 0.12$, $C_{\rm b} = 2200\,\mu$F, $C_{hv} = 330\,\mu$F, $d_2 = 0.572$, $V_{\rm b} = 300$ V and $R = 80\,\Omega$, the transfer functions $G_{i_{bd}}(s)$, $G_{v_{hd}}(s)$ and $G_{v_{\rm h}i_{\rm b}}(s)$ will be

$$G_{i_{\rm b}d}(s) = \frac{1.68\times10^{7}s^{2} + 1.289\times10^{10}s + 2.26\times10^{12}}{s^{3} + 4.815\times10^{5}s^{2} + 6.488\times10^{7}s + 5.33\times10^{10}} \tag{31}$$

$$G_{v_{\rm h}d}(s) = \frac{3.227\times10^{7}s^{2} + 6.958\times10^{10}s + 2.564}{s^{3} + 4.815\times10^{5}s^{2} + 6.488\times10^{7}s + 5.33\times10^{10}} \tag{32}$$

$$G_{v_{\rm h}i_{\rm b}}(s) = \frac{3.227\times10^{7}s^{2} + 6.958\times10^{10}s + 2.56\times10^{12}}{1.68\times10^{7}s^{2} + 6.488\times10^{10}s + 2.26\times10^{12}} \tag{33}$$

The stability analysis of the PR mode (inner current loop and outer voltage loop) is investigated using the transfer function $G_{i_{\rm b}d}(s)$ and $G_{v_{\rm h}i_{\rm b}}(s)$. The parameters of the PI controller (inner and outer) have been selected using the pole-zero placement technique. A fine tuning of the controller parameters is performed using the MATLAB SISO tool to ensure stability margins. Fig. 10*a* shows the frequency response of inner current loop with and without controllers, where $G_c(s)$ is transfer function of inner current PI controller.

The bandwidth of inner loop gain ($G_c(s)G_{i_{\rm b}d}$(s)) is kept around 6000 rad/s, which is one-twentieths of the switching frequency (20 kHz). To confirm the stable operation and fast transient response, the phase margin of inner loop gain is selected as 47°. The frequency response of outer loop with and without controllers has been shown in Fig. 10*b*. The bandwidth of outer loop gain ($G_{v_{\rm h}i_{\rm b}}$(s)) is kept around 600 rad/s, which is one-tenth of bandwidth of inner loop gain and phase margin is around 90°. Similarly, the stability analysis of front-end converter (plug-in charging mode (two-order system)) can also be illustrated. In this mode, one loop (current controller) control strategy has been used for the battery charging. In a single-phase system, a second harmonic ripple appears in the output. To prevent the presence of second harmonic ripple in the input current, the bandwidth of current loop gain is kept below 100 Hz, which is shown in Fig. 11.

## 4 Results and discussions

The developed system is simulated in Matlab/Simulink environment and its performance is studied in details with the parameters provided in Table 5.

The various waveforms captured in the plug-in charging mode are illustrated in Fig. 12. In this operating mode, the utility grid is

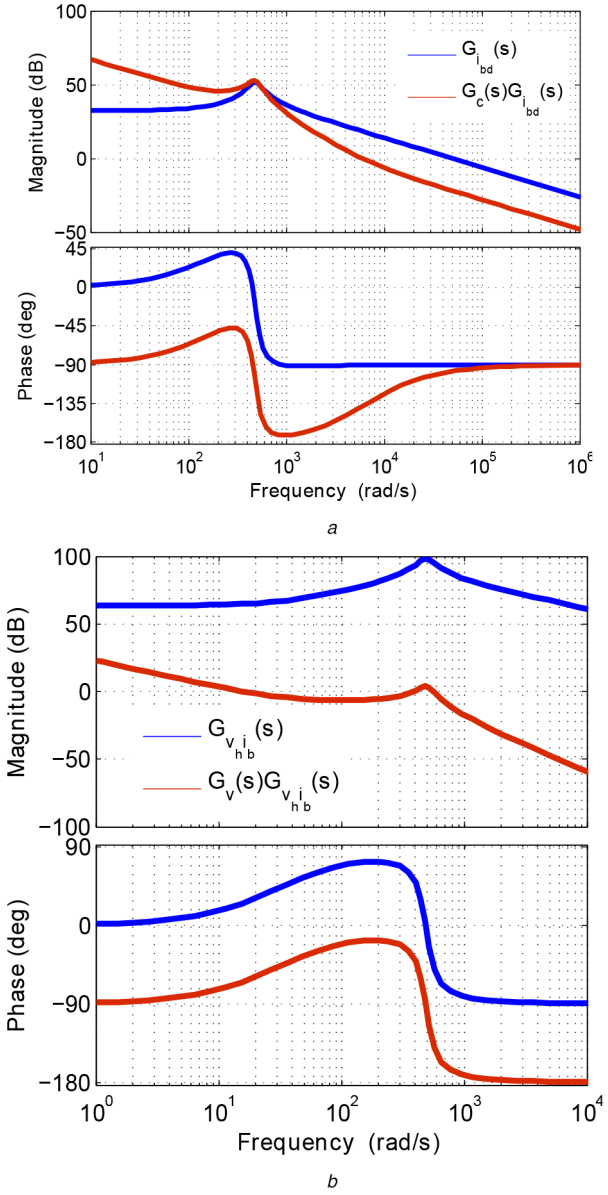


**Fig. 10** *Bode diagrams of PR mode*
***(a)*** Open loop and loop gain plot of inner current loop, ***(b)*** Outer voltage loop

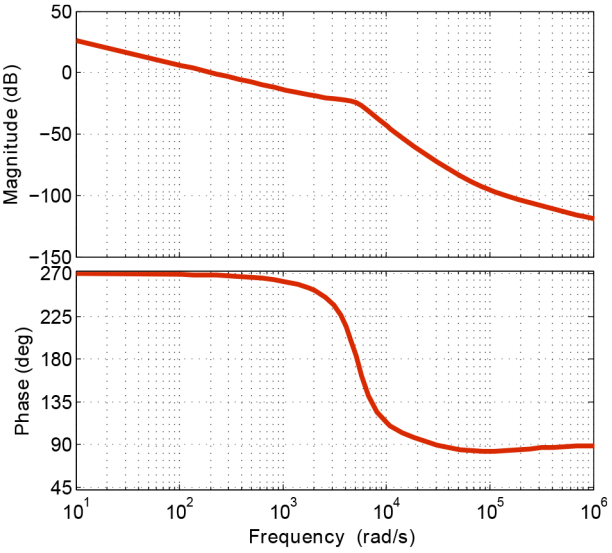


**Fig. 11** *Bode plot of loop gain during the plug-in charging mode*

used to charge the battery and the developed control for the proposed converter manages the power quality at the grid side. The

**Table 5** Parameters for the simulation study

| Parameters | Value |
|---|---|
| DC-link/grid voltage $V_{hv}/v_g$ | 400/220 V |
| battery voltage ($V_b$) | 300 V |
| nominal charging power ($P_b$) | 1.2 kW |
| line frequency ($f_L$) | 50 Hz |
| switching frequency ($f_s$) | 20 kHz |
| battery capacity | 26 Ah |

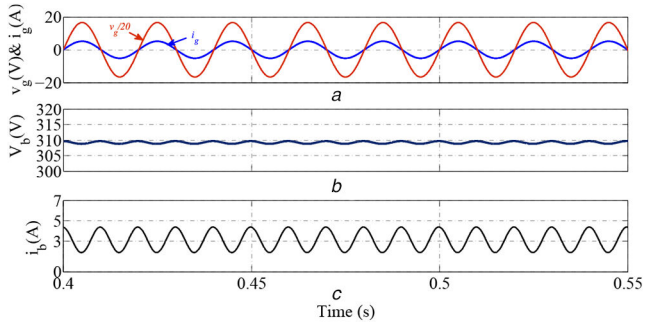


**Fig. 12** *Simulation results during the plug-in charging operation*
***(a)*** Grid voltage and current, ***(b)*** Battery voltage, ***(c)*** Battery current

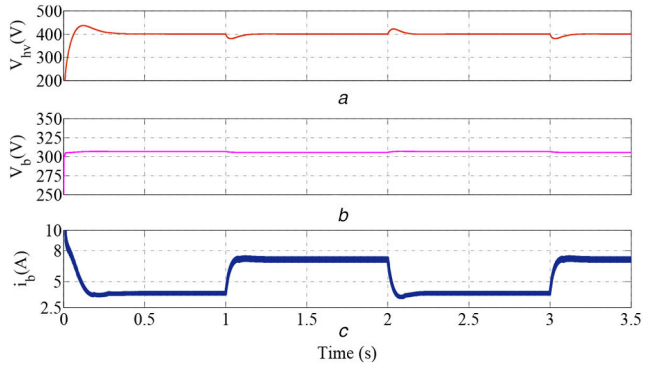


**Fig. 13** *Simulated waveforms during the PR mode*
***(a)*** DC-link voltage, ***(b)*** Battery voltage, ***(c)*** Battery current

in-phase nature of grid voltage and current having perfectly sinusoidal shape, as shown in Fig. 12*a* demonstrate the unity power factor (UPF) operation at the grid side. The nature of battery voltage and current at 20% SOC condition are shown in Figs. 12*b* and *c*, respectively. The oscillation at the low frequency 100 Hz in the battery current is observed in Fig. 12*c*. This oscillation is due to inherent single-stage charging connection and, therefore, the magnitude of peak-to-peak battery current ripple can be twice of the average value of battery current. Alhough, this 100 Hz ripple present in the battery current can be mitigated by including one small value of filter inductor in the path of battery current. The size of this filter is governed by the class of battery and charging system compactness. The value of grid current and average battery current at 1.2 kW charging power observed in Fig. 12 are 5.8 and 3.90 A, respectively.

The behaviour of system parameters under the PR mode (i.e. driving mode), is represented in Fig. 13. In this operating mode, the energy stored in the battery by the plug-in charging mode is used to accelerate the vehicle through charging the DC-link capacitor. The PR mode control regulates the DC-link voltage, $V_{hv}$ constant, i.e. 400 V and it is also requisite to smoothly operate the system. The dynamic behaviour of system and the effectiveness of developed control under this situation is verified with a step load change, as presented in Fig. 13. At $t$ = 1 s, load power is increment from 1 to 2 kW and again decreased to 1 kW at $t$ = 2 s. The load power again increased to 2 kW at $t$ = 3 s. The successful regulation of DC-link voltage, i.e. 400 V at a desired value under these load changes is demonstrated in Fig. 13*a*, whereas the corresponding variation in

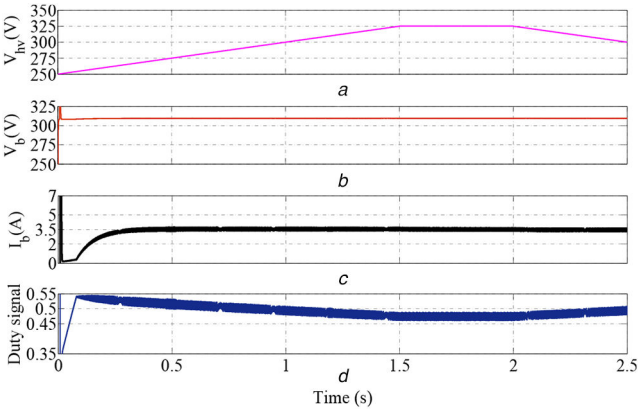


**Fig. 14** *Simulated waveforms during the RB mode*
***(a)*** DC-link voltage, ***(b)*** Battery voltage, ***(c)*** Battery current, ***(d)*** Duty signal

**Table 6** Parameters for the experimentation study

| Parameters | Value |
|---|---|
| DC-link/grid voltage $V_{hv}/v_g$ | 80/55 V |
| battery voltage ($V_b$) | 48 V |
| nominal charging power ($P_b$) | 120 W |
| line frequency ($f_L$) | 50 Hz |
| switching frequency ($f_s$) | 20 kHz |
| battery capacity | 26 Ah |

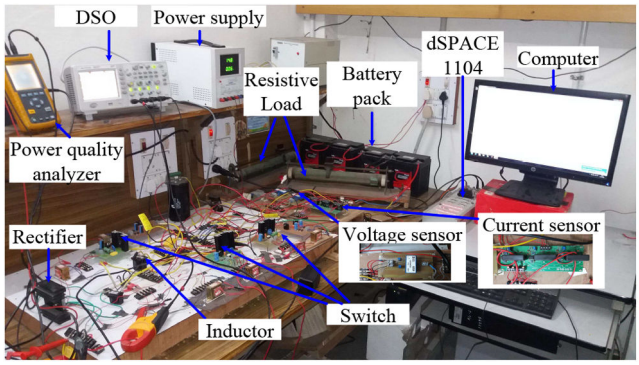


**Fig. 15** *Photo of experimental setup*

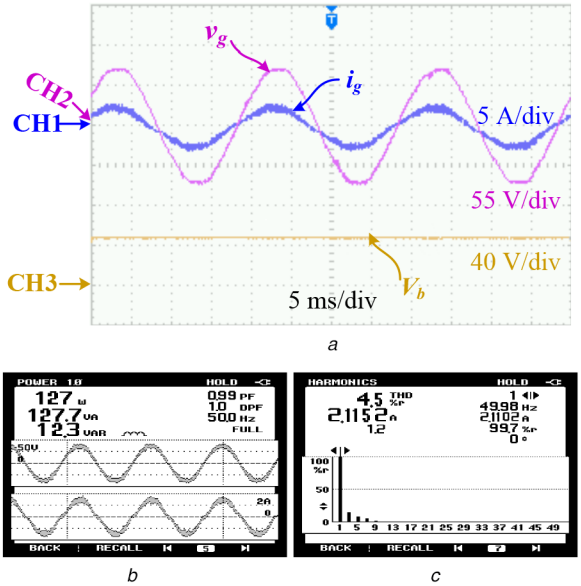


**Fig. 16** *Experimental results during the plug-in charging*
***(a)*** Waveforms of grid voltage, grid current and battery voltage, ***(b)*** Measured powers and power factor at grid side, ***(c)*** Harmonic spectrum of grid current

battery voltage and current are represented in Figs. 13*b* and *c*, respectively. The observed magnitude of battery current for 1 and 2 kW loads are around 3.4 and 6.9 A, respectively.

The simulated response of developed system when braking energy is used back to charge the battery is shown in Fig. 14. This mode is realised varying the DC-link voltage linearly from 250 to 325 V and then preserved at 325 V between $t$ = 1.5 s and $t$ = 2 s then further decreased linearly to 300 V, as demonstrated in Fig. 14*a*. It is noted from Fig. 14*c* that the charging current of battery is of magnitude equal to 3.5 A current. The variation in the duty ratio of the proposed converter is presented in Fig. 14*d*. The successful buck and boost operation capability of the proposed converter is authenticated by the variation of duty ratio both higher and lower than 0.5. The value of duty ratio goes above 0.5 when the battery voltage is higher than the DC-link voltage and comes below 0.5 when the DC-link voltage is higher than the battery voltage.

The real-time performance of the proposed EV charging system is validated by a developed prototype and the improved performance of the proposed charging system is confirmed with captured results. The parameters for experimental validation are given in Table 6. The developed hardware set-up in a laboratory is shown in Fig. 15. The MOSFET switch (IRP460) operated at 20 kHz is used in the proposed converter and its gate driver circuit is made-up of TLP-250 optocoupler. A field-programmable gate array (FPGA)-based dSPACE-1104 controller is used to implement the software to the develop hardware and to provide the high-frequency PWM pulses to the MOSFET switch of the proposed converter. The fast recovery diode MUR-1560 is used as a body diode of MOSFET switch to minimise the RRV reverse recovery losses (RRV) and eliminate the undesirable transients of the circuit.

The voltage is sensed through an AD202JN-based isolation amplifier. To sense the DC current at different parts of the converter circuit, Hall effect current sensors TELCON HTP-25 are used. Four modules of exide power safe plus sealed lead acid battreies of 12 V are used to verify each mode of operation. The various saveforms are captured utilising Agilent DSO1014A and Fluke manufactured power quality analyser. The real-time performance of system parameters in the plug-in charging mode is demonstrated in Fig. 16. The captured characteristics of grid current ($i_g$) and grid voltage ($v_g$) at 120 W charging power are illustrated in Fig. 16*a*. It is observed from Fig. 16*a* that both $i_g$ and $v_g$ are in-phase and have perfectly sinusoidal nature, which verified the UPF operation. This UPF operation offers a minimum burden and minimise the electricity consumption from the grid. The power quality parameters are also shown in Figs. 16*b* and *c*. The measured THD in the grid current is 4.5% which is within international standard: IEC 61000-3-2 and measured power factor of the converter is 0.999.

Fig. 17 shows the waveforms of the plug-in charging mode using NLCC method. The nature of current through the switch $S_1$ is illustrated at CH1. The integral of this current produces a parabolic signal, $v_i$ then the signal $v_i$ is inverted by multiplying with a negative signal having unity magnitude as $-v_i$. Further, the resultant signal is compared with a reference carrier signal, $v_c$. Whenever, the magnitude of $v_i$ is higher than $-v_i$, there is a generation of high PWM signal for $S_1$. The $v_c$ is clinched at a fixed magnitude to inhibit it from achieving an infinite value at the starting of switching cycles.

The behaviour of various parameters in the PR mode with 80 V DC-link (CH1) and 48 V battery voltage (CH2) are illustrated in Fig. 18*a*. The dynamic performance of developed PEVs charging system in this operation mode is realised and examined by varying step load from 85 to 130 W and again from 130 to 85 W. Fig. 18*b* shows the corresponding variation in the battery voltage and current, which are shown at CH2 and CH3, respectively. The efficacy of implemented control technique to regulate the DC-link voltage at 80 V under variation in loads is demonstrated in Fig. 18*b*. The estimated battery powers are 90.24 and 138.72 W at 85 and 130 W loads, respectively.

The energy generated through the braking process of vehicle drive is utilised to charge the battery in the regenerative braking mode will increase driving distance per unit charge. Since, the DC-

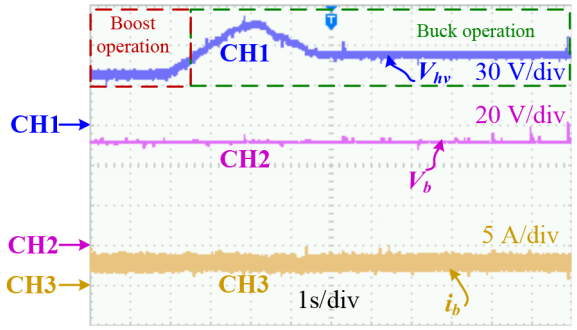


**Fig. 17** *Control signal waveforms during the plug-in charging mode*

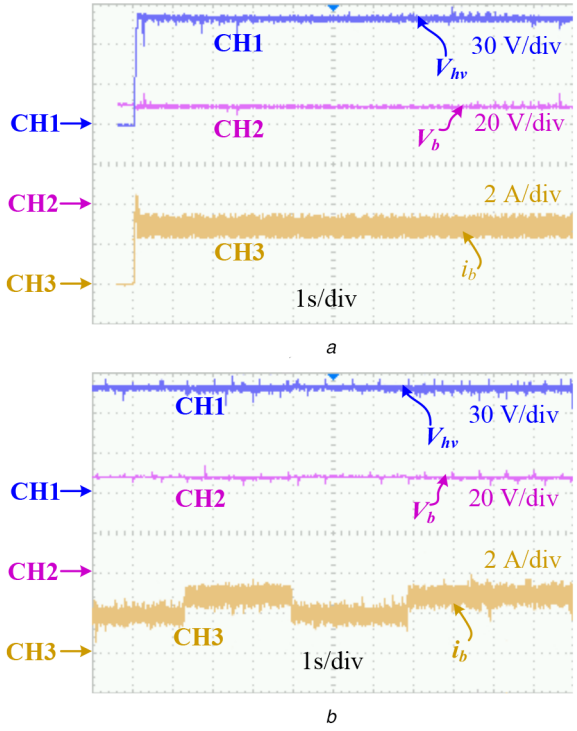


**Fig. 18** *Experimental results during the PR mode*
***(a)*** Dynamic operation of PR mode, ***(b)*** Closed-loop verification of RB mode

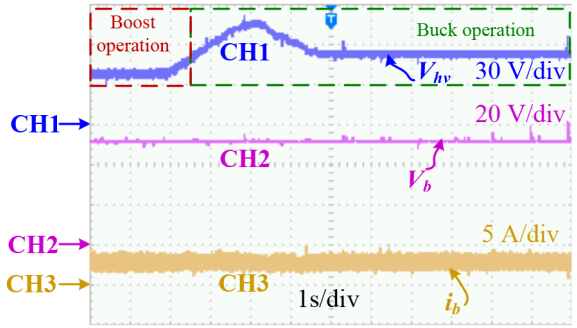


**Fig. 19** *Closed-loop verification of the RB mode*

link variation is directly related to the drive speed, therefore, the dynamic performance of developed system in this mode is tested by changing the magnitude of DC-link voltage. The DC-link voltage changes from 36 to 80 V at CH1, meanwhile the charging current is regulated at 2.5 A, as displayed in Fig. 19 at CH3.

## 5 Conclusion

In this work, a compact non-isolated DC–DC converter with NLCC has been proposed for on-board applications of PEVs. The implemented NLCC technique minimises the size and complexity of feedback circuitry required for PFC at the grid side and therefore, offers the compactness of power-train for EVs. The proposed converter is basically a single-stage configured DC–DC converter, which is capable to take care of all three modes: plug-in charging, PR and RB modes, which removes the requirement of extra inductor and switches (because a single converter operates for all modes) for built-in electric power-train, and improves the volumetric power density of the electric power-train. The aforementioned advantages of the proposed system are desirable for light EVs (LEVs), such as e-scooters (standing/self-balancing and folding types), e-bikes, e-golf carts, e-rickshaws, and other types of e-three-wheelers. A detailed analysis of the peak voltage/current stresses together with loss analysis of the proposed configuration has been investigated to appropriately select the power-stage switches. The maximum efficiencies of the converter in plug-in charging, PR and RB modes are observed as 94.6, 96.9 and 97.2%, respectively.

## 6 References


[1] Li, G., Zhang, X.P.: 'Modeling of plug-in hybrid electric vehicle charging demand in probabilistic power flow calculations', *IEEE Trans. Smart Grid*, 2012, **3**, (1), pp. 492–499

[2] Emadi, A., Lee, Y.J., Rajashekara, K.: 'Power electronics and motor drives in electric, hybrid electric, and plug-in hybrid electric vehicles', *IEEE Trans. Ind. Electron.*, 2008, **55**, (6), pp. 2237–2245

[3] Musavi, F., Eberle, W., Dunford, W.G.: 'A high-performance single-phase bridgeless interleaved pfc converter for plug-in hybrid electric vehicle battery chargers', *IEEE Trans. Ind. Appl.*, 2011, **47**, (4), pp. 1833–1843

[4] Oh, C.Y., Kim, D.H., Woo, D.G., *et al.*: 'A high-efficient nonisolated single-stage on-board battery charger for electric vehicles', *IEEE Trans. Power Electron.*, 2013, **28**, (12), pp. 5746–5757

[5] Singh, A.K., Pathak, M.K.: 'An improved two-stage non-isolated converter for on-board plug-in hybrid EV battery charger'. 2016 IEEE 1st Int. Conf. on Power Electronics,Intelligent Control and Energy Systems (ICPEICES), Delhi, India, 2016, pp. 1–6

[6] Yilmaz, M., Krein, P.T.: 'Review of battery charger topologies, charging power levels, and infrastructure for plug-in electric and hybrid vehicles', *IEEE Trans. Power Electron.*, 2013, **28**, (5), pp. 2151–2169

[7] Onar, O.C., Kobayashi, J., Erb, D.C., *et al.*: 'A bidirectional high-power-quality grid interface with a novel bidirectional noninverted buck-boost converter for PHEVs', *IEEE Trans. Veh. Technol.*, 2012, **61**, (5), pp. 2018–2032

[8] Bendien, J.C., Fregien, G., van Wyk, J.D.: 'High-efficiency on-board battery charger with transformer isolation, sinusoidal input current and maximum power factor', *IEE Proc. B - Electr. Power Appl.*, 1986, **133**, (4), pp. 197–204

[9] Pahlevaninezhad, M., Das, P., Drobnik, J., *et al.*: 'A new control approach based on the differential flatness theory for an AC/DC converter used in electric vehicles', *IEEE Trans. Power Electron.*, 2012, **27**, (4), pp. 2085–2103

[10] Verma, A.K., Singh, B., Shahani, D.T.: 'Grid to vehicle and vehicle to grid energy transfer using single-phase bidirectional ac-dc converter and bidirectional dc-dc converter'. 2011 Int. Conf. on Energy, Automation and Signal, Bhubaneswar, Odisha, India, 2011, pp. 1–5

[11] Shi, C., Wang, H., Dusmez, S., *et al.*: 'A SiC-based high-efficiency isolated onboard pev charger with ultrawide dc-link voltage range', *IEEE Trans. Ind. Appl.*, 2017, **53**, (1), pp. 501–511

[12] Bist, V., Singh, B.: 'A brushless dc motor drive with power factor correction using isolated zeta converter', *IEEE Trans. Ind. Inf.*, 2014, **10**, (4), pp. 2064–2072

[13] Bist, V., Singh, B.: 'An adjustable-speed PFC bridgeless buck -boost converter-fed bldc motor drive', *IEEE Trans. Ind. Electron.*, 2014, **61**, (6), pp. 2665–2677

[14] Patil, D., Agarwal, V.: 'Compact onboard single-phase EV battery charger with novel low-frequency ripple compensator and optimum filter design', *IEEE Trans. Veh. Technol.*, 2016, **65**, (4), pp. 1948–1956

[15] Egan, M.G., O'Sullivan, D.L., Hayes, J.G., *et al.*: 'Power-factor-corrected single-stage inductive charger for electric vehicle batteries', *IEEE Trans. Ind. Electron.*, 2007, **54**, (2), pp. 1217–1226

[16] Kong, P.Y., Aziz, J.A., Sahid, M.R., *et al.*: 'A bridgeless PFC converter for on-board battery charger'. 2014 IEEE Conf. on Energy Conversion (CENCON), Johor Bahru, Malaysia, 2014, pp. 383–388

[17] Aharon, I., Kuperman, A.: 'Topological overview of powertrains for battery-powered vehicles with range extenders', *IEEE Trans. Power Electron.*, 2011, **26**, (3), pp. 868–876

[18] Ahmed, A., Khan, M.A., Badawy, M., *et al.*: 'Performance analysis of bi-directional dc-dc converters for electric vehicles and charging infrastructure'. 2013 IEEE Energy Conversion Congress and Exposition, Denver, CO, USA, 2013, pp. 1401–1408

[19] Park, T., Kim, T.: 'Novel energy conversion system based on a multimode single-leg power converter', *IEEE Trans. Power Electron.*, 2013, **28**, (1), pp. 213–220

[20] Qian, W., Cha, H., Peng, F.Z., *et al.*: '55-kW variable 3X DC-DC converter for plug-in hybrid electric vehicles', *IEEE Trans. Power Electron.*, 2012, **27**, (4), pp. 1668–1678

[21] Lee, Y.J., Khaligh, A., Emadi, A.: 'Advanced integrated bidirectional AC/DC and DC/DC converter for plug-in hybrid electric vehicles', *IEEE Trans. Veh. Technol.*, 2009, **58**, (8), pp. 3970–3980

[22] Dusmez, S., Khaligh, A.: 'A compact and integrated multifunctional power electronic interface for plug-in electric vehicles', *IEEE Trans. Power Electron.*, 2013, **28**, (12), pp. 5690–5701
[23] Singh, A.K., Pathak, M.K.: 'Single-phase bidirectional ac/dc converter for plug-in electric vehicles with reduced conduction losses', *IET Power Electron.*, 2018, **11**, (1), pp. 140–148
[24] Dusmez, S., Khaligh, A.: 'A charge-nonlinear-carrier-controlled reduced-part single-stage integrated power electronics interface for automotive applications', *IEEE Trans. Veh. Technol.*, 2014, **63**, (3), pp. 1091–1103
[25] Singh, A.K., Pathak, M.K.: 'Single-stage zeta-sepic-based multifunctional integrated converter for plug-in electric vehicles', *IET Electr. Syst. Transp.*, 2018, **8**, (2), pp. 101–111
[26] Cocconi, assigneeA.G.: 'Combined motor drive and battery recharge system'. 5 341 075, 1994
[27] Rippel, assigneeW.E.: 'Integrated traction inverter and battery charger apparatus'. 4 920 475, 1990
[28] Tang, Y., Zhu, D., Jin, C., *et al.*: 'A three-level quasi-two-stage single-phase PFC converter with flexible output voltage and improved conversion efficiency', *IEEE Trans. Power Electron.*, 2015, **30**, (2), pp. 717–726
[29] Chinmaya, K.A., Singh, G.K.: 'A single-stage integrated charger for electric vehicles (evs) and plug - in electric vehicles (pevs) incorporating induction motor drive'. 44th Annual Conf. of the IEEE Industrial Electronics Society (IECON 2018), Washington, DC, USA, 2018, pp. 954–959
[30] Singh, A.K., Pathak, M.K.: 'A multi-functional single-stage power electronic interface for plug-in electric vehicles application', *Electr. Power Compon. Syst.*, 2018, **46**, (2), pp. 135–148
[31] Patil, D., Sinha, M., Agarwal, V.: 'A cuk converter based bridgeless topology for high power factor fast battery charger for electric vechicle application'. 2012 IEEE Transportation Electrification Conf. and Expo (ITEC), Dearborn, MI, USA, 2012, pp. 1–6
[32] Singh, A.K., Pathak, M.K., Rao, Y.S.: 'A multi-device front-end power factor converter for ev battery charger'. 2017 3rd Int. Conf. on Computational Intelligence Communication Technology (CICT), Ghaziabad, India, 2017, pp. 1–6
[33] Pahlevaninezhad, M., Das, P., Drobnik, J., *et al.*: 'A ZVS interleaved boost AC/DC converter used in plug-in electric vehicles', *IEEE Trans. Power Electron.*, 2012, **27**, (8), pp. 3513–3529
[34] Bai, H., Zhang, Y., Semanson, C., *et al.*: 'Modelling, design and optimisation of a battery charger for plug-in hybrid electric vehicles', *IET Electr. Syst. Transp.*, 2011, **1**, (1), pp. 3–10
[35] Morcos, M.M., Dillman, N.G., Mersman, C.R.: 'Battery chargers for electric vehicles', *IEEE Power Eng. Rev.*, 2000, **20**, (11), pp. 8–11
[36] Mahdavi, M., Farzanehfard, H.: 'Bridgeless SEPIC PFC rectifier with reduced components and conduction losses', *IEEE Trans. Ind. Electron.*, 2011, **58**, (9), pp. 4153–4160
[37] Kim, T.H., Jeong, J.B., Lee, B.H., *et al.*: 'Analytical study on low-frequency ripple effect of battery charging'. 2012 IEEE Vehicle Power and Propulsion Conf., Seoul, Republic of Korea, 2012, pp. 809–811
[38] Singh, S., Singh, B., Bhuvaneswari, G., *et al.*: 'Power factor corrected zeta converter based improved power quality switched mode power supply', *IEEE Trans. Ind. Electron.*, 2015, **62**, (9), pp. 5422–5433
[39] Vlatkovic, V., Borojevic, D., Lee, F.C.: 'Input filter design for power factor correction circuits', *IEEE Trans. Power Electron.*, 1996, **11**, (1), pp. 199–205
[40] Jang, Y., Jovanovic, M.M.: 'Interleaved boost converter with intrinsic voltage-doubler characteristic for universal-line PFC front end', *IEEE Trans. Power Electron.*, 2007, **22**, (4), pp. 1394–1401
[41] Tang, W., Lee, F.C., Ridley, R.B.: 'Small-signal modeling of average current-mode control', *IEEE Trans. Power Electron.*, 1993, **8**, (2), pp. 112–119
[42] Sen, G., Elbuluk, M.E.: 'Voltage and current-programmed modes in control of the z-source converter', *IEEE Trans. Ind. Appl.*, 2010, **46**, (2), pp. 680–686
[43] Youn, H.S., Park, J.S., Park, K.B., *et al.*: 'A digital predictive peak current control for power factor correction with low-input current distortion', *IEEE Trans. Power Electron.*, 2016, **31**, (1), pp. 900–912
[44] Raviraj, V.S.C., Sen, P.C.: 'Comparative study of proportional-integral, sliding mode, and fuzzy logic controllers for power converters', *IEEE Trans. Ind. Appl.*, 1997, **33**, (2), pp. 518–524
[45] Marvi, M., Fotowat-Ahmady, A.: 'A fully ZVS critical conduction mode boost pfc', *IEEE Trans. Power Electron.*, 2012, **27**, (4), pp. 1958–1965
[46] Erickson, M.D.R.W.: '*Fundamental of power electronics*' (Springer, New Delhi, 2005)